A high-temperature x-ray absorption spectroscopy study of ReO_3

1996 J. Phys.: Condens. Matter 8 9083

(http://iopscience.iop.org/0953-8984/8/46/013)

J. Phys.: Condens. Matter **8** (1996) 9083–9102. Printed in the UK

A high-temperature x-ray absorption spectroscopy study of ReO_3

A Kuzmin†‡, J Purans†, G Dalba§, P Fornasini§ and F Rocca‡

† Institute of Solid State Physics, University of Latvia, LV-1063 Riga, Latvia

‡ Centro CNR-ITC di Fisica degli Stati Aggregati ed Impianto Ionico, I-38050 Povo (Trento), Italy

§ Istituto Nazionale di Fisica della Materia, Dipartimento di Fisica, Università di Trento, I-38050 Povo (Trento), Italy

Received 9 July 1996

Abstract. We present for the first time a high-temperature x-ray absorption spectroscopy study of ReO_3 at the Re L_3 edge. The analysis both of the XANES and of the EXAFS regions shows that, in ReO_3, a progressive localization of the 5d states following the temperature rise is accompanied at $T > 350$ K by a distortion of the ReO_6 octahedra, which increases up to the ReO_3 decomposition temperature $T_d \simeq 673$ K. The distortion leads to the lowering of the rhenium site symmetry from $O_h (T \leqslant 350\ \text{K}) \rightarrow D_{4h} (T \simeq 513\ \text{K}) \rightarrow C_{4v} (T \simeq 668\ \text{K})$ and is due to the electron–phonon coupling of the 5d electrons with the M_3 and M_3^{rZ} phonons and to the Jahn–Teller effect caused by the rhenium $5d^1$ electron which becomes localized at high temperature.

1. Introduction

The physical properties of transition metal (TM) oxide materials are mainly determined by the outer-shell electrons, among which the d electrons of metal ions have the greatest importance [1]. The d electrons can be found in localized and/or collective states and, in some cases, the transition from one state to another can be induced. The intermediate character of the d electrons is due to the fact that they are not screened from the neighbouring ions by outer s and p core electrons [1]. Besides, the d electrons are characterized by strong correlations and by electron–phonon coupling, leading to a different degree of local lattice distortions [1, 2]. Thus, thanks to their properties, the d electrons are responsible for a large number of effects occurring in TM oxides: high-T_c superconductivity [3], ferroelectric and other phase transitions [4], charge-density waves (CDW) [5] and so on.

Rhenium trioxide (ReO_3) is a TM oxide with a unique perovskite-like structure (ABO_3) composed of ReO_6 octahedra joined by corners with the A sites being vacant [6]. Rhenium atoms are located at the centres of the octahedra and oxygen atoms at their vertices. In many perovskites, such as $SrTiO_3$, $BaTiO_3$ and $KNbO_3$, the condensation of one or more optical modes causes a re-arrangement of the local electronic and atomic structures and consequent structural phase transitions [4]. In contrast, the structure of ReO_3 is non-distorted at atmospheric pressure down to liquid-helium temperature [7]. Since ReO_3 has metallic conductivity below 500 K [8], the stability of its cubic lattice was explained in terms of the suppression of the screening effect on the lattice vibrations [1, 7]: here the screening is not free-electron-like as in simple metals but has an atomic (rhenium 5d and oxygen 2p) character.

0953-8984/96/469083+20$19.50

However, a sequence of pressure-induced phase transitions $Pm3m \rightarrow P4/mbm \rightarrow I4/mmm \rightarrow Im3$ was found in ReO_3 at room temperature (RT) starting from 5 kbar [9, 10]. These transitions are related to the condensation of M_3 modes and consist of successive rotations of the *rigid* ReO_6 octahedra around [100] axes [10]. Only small distortion of the ReO_6 octahedra, resulting in two short 1.875 Å and four long 1.8707 Å Re–O distances, was found at 5.2 kbar in the tetragonal $P4/mbm$ phase by neutron powder diffraction [10]. A similar sequence of phase transitions had been observed earlier upon cooling from 500 to 3 K in the metallic perovskite Na_xWO_3 ($x > 0.5$) by x-ray diffraction (XRD) [11] and low-frequency Raman measurements [12]. Note that, as in ReO_3, the WO_6 octahedra in Na_xWO_3 ($x > 0.5$) are also considered to be rigid [12].

Our previous x-ray absorption spectroscopy (XAS) studies of ReO_3 at the Re L_3 edge agree well with the absence of any local distortion around rhenium atoms at atmospheric pressure in the temperature range from 77 K to RT [13–15]. We point out that XAS is an accurate local probe insensitive to the presence of long-range order, therefore it provides information complementary to that available from diffraction techniques.

In this work we present for the first time the results of a high-temperature XAS study of ReO_3. They show evidence of a progressive 5d electron localization at rhenium sites which is accompanied at $T > 350$ K by a distortion of the ReO_6 octahedra, increasing up to the ReO_3 decomposition temperature $T_d \simeq 673$ K [16].

The paper is organized as follows: in section 2, the experimental procedure of the x-ray absorption measurements at the Re L_3 edge in ReO_3 is described; in section 3, data treatment procedures used in the analysis are discussed; in section 4, the results of the XANES and EXAFS analyses are presented; in section 5, we discuss the possible model being able to explain the high-temperature behaviour of ReO_3; in section 6, a summary of the present work and the main conclusions are given.

2. Experimental details

X-ray absorption spectra of the Re L_3 edge in ReO_3 were recorded in transmission mode at the LURE DCI storage ring (Orsay, France) on the D13 bending-magnet beamline (EXAFS-3). The electron energy was 1.85 GeV and the maximum stored current 312 mA. A standard transmission scheme with a Si(311) double-crystal monochromator de-tuned to 50% of intensity for harmonic rejection and two ion chambers containing argon gas was used. The data were recorded during a single injection of the storage ring with an energy spacing of 2 eV, count rate 2 s per point and energy resolution about 3 eV achieved with a 0.7 mm vertical slit. Special attention was paid to the linearity of the ionization chamber response. The sample for x-ray absorption measurements was prepared from commercial 99.9% polycrystalline ReO_3 (Metalli Preziosi SpA) whose quality was checked by x-ray powder diffraction. ReO_3 was finely ground and mechanically mixed with boron nitride powder. The mixture was placed in a boron nitride cell mounted in a furnace. The obtained sample thickness corresponded to an absorption jump $\Delta\mu \simeq 1.4$ at the Re L_3 edge. The temperature was varied within the range from RT to 670 K and stabilized within ± 2 K during each measurement. No change in the absorption jump was observed in the temperature range from RT to 643 K; however, it decreased by about 30% to $\Delta\mu \simeq 1.0$ for the last spectrum measured at $T = 668$ K, close to the ReO_3 decomposition temperature $T_d \simeq 673$ K [16]. The normalized x-ray absorption near-edge structures (XANES) at several temperatures are shown in figure 1(a).

Low-temperature measurements (from 77 to 350 K) of the Re L_3 edge in ReO_3 had previously been performed in transmission mode at the ADONE storage ring (Frascati,

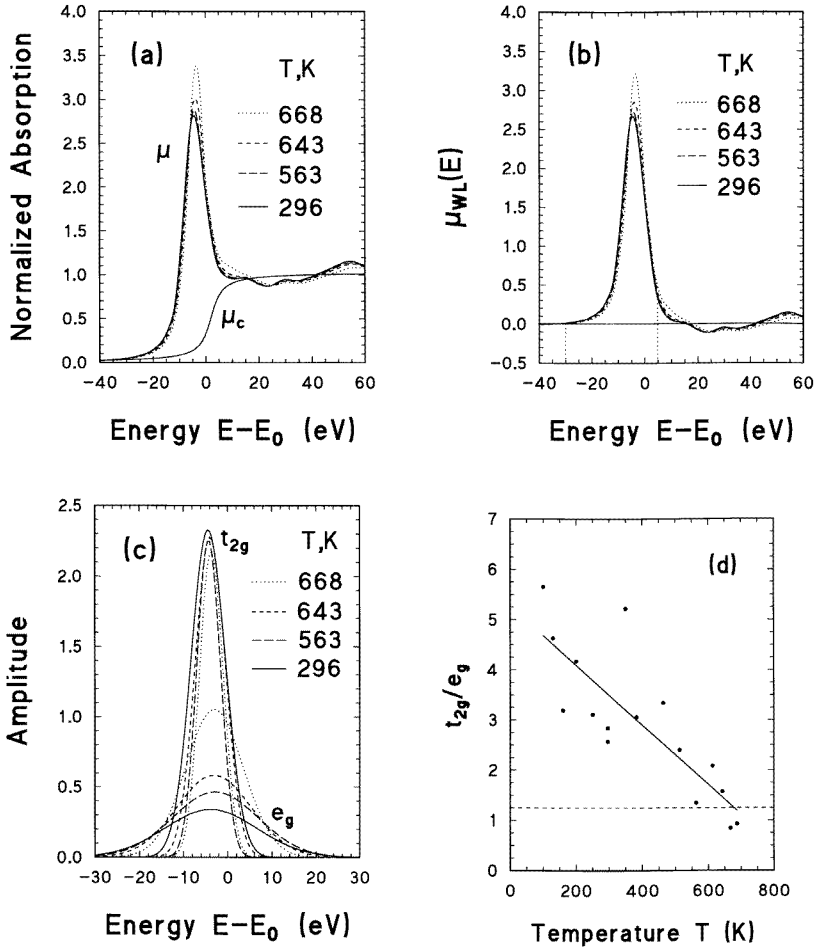

Figure 1. (a) Normalized XANES spectra $\mu(E)$ at the Re L_3 edge in ReO_3. The variation of the white-line intensity and position with the temperature increase is clearly visible. $\mu_c(E)$ is the contribution of transitions from the $2p_{3/2}$(Re) level to the continuum of the unoccupied free-electron-like states given by equation (5). (b) $\mu_{WL}(E) = \mu(E) - \mu_c(E)$. The vertical dotted lines show the range of the integration used to obtain the WL area. (c) The variation of two Gaussian components describing the WL with the temperature increase. The narrow higher curves correspond to the $t_{2g}(\pi^*)$ sub-band and the broad lower curves to the $e_g(\sigma^*)$ sub-band. The amplitude scale is the same as in figure 1(b). (d) The temperature-dependence of the ratio $|\langle t_{2g}(\pi^*)|\hat{\epsilon}\cdot\boldsymbol{r}|2p_{3/2}\rangle|^2 N_{t_{2g}(\pi^*)}(E)/|\langle e_g(\sigma^*)|\hat{\epsilon}\cdot\boldsymbol{r}|2p_{3/2}\rangle|^2 N_{e_g(\sigma^*)}(E)$ showing the variation in the number of free states and the degree of localization for the two sub-bands. The broken line corresponds to the completely localized orbitals (atomic case) with the number of unoccupied states equal to five in t_{2g} and four in e_g.

Italy) on the PWA-BX2 wiggler beamline. Their details and analysis have been published by us elsewhere [15]. A comparison between the two sets of data, measured at different experimental sites (ADONE and DCI), showed that they differ slightly in the experimental resolution. Using the room-temperature spectrum available in both sets of data, we found that this difference can be compensated by convolution of the spectra measured at ADONE with a Lorentzian curve having the full width at half maximum (FWHM) 1.7 eV. This

procedure was applied to the whole set of spectra from [15] to allow a meaningful comparison with the present high-temperature measurements. Note that no change in the values of the structural parameters was observed for the corrected set of spectra in comparison with the previous results [15]. It was also checked that the used correction procedure does not affect the results of the decomposition of the Re L_3 edge XANES into two components, discussed in section 3.1.

3. Data analysis

3.1. XANES

The experimental Re L_3 edge XANES spectrum (figure1(a)) consists of a prominent peak, the so-called 'white line' (WL), located just above the absorption edge and a fine structure which is located above the WL and is due to the scattering of the photoelectron by atoms surrounding the absorber.

The part of the XANES spectra $\mu_{WL}(E)$ related to the WL was singled out by subtracting from the total normalized absorption $\mu(E)$ the contribution $\mu_c(E)$ of transitions from the $2p_{3/2}$(Re) level to the continuum of the unoccupied free-electron-like states in the absence of the surrounding atoms, figure 1(a). The contribution $\mu_c(E)$ is defined as [17]

$$\mu_c(E) = \tfrac{1}{2} + (1/\pi)\tan^{-1}[2(E - E_0)/\Delta] \tag{1}$$

where the position of E_0, related to the energy of the continuum threshold, was chosen in the usual way [13–15] as shown in figure 1(a) and Δ depends on the experimental broadening and on the lifetime of the photo-absorption process [17]: it can be roughly chosen in such a way as to give a slope of $\mu_c(E)$ in the vicinity of E_0 equal to the slope of the experimental $\mu(E)$ close to the absorption edge. The amplitude and the area of the WL and the position of the WL maximum were determined from $\mu_{WL}(E)$ in the energy range from -30 to 5 eV relative to the E_0 position (figure 1(b)). Their variations with temperature are shown in figure 2 and will be discussed in section 4.1.

The WL (see figure 1(b)) in ReO_3 corresponds to the unoccupied states in the 5d(Re)–2p(O) conduction band split by the crystal field of six oxygen atoms. It was found that the WL cannot be described by a single Gaussian or Lorentzian function. However, a model consisting of two Gaussians gives excellent results. The obtained Gaussian components are shown in figure 1(c), in which the higher set of narrow Gaussian curves (G_t) is attributed to the $t_{2g}(\pi^*)$ sub-band and the lower set of broad Gaussian curves (G_e) to the $e_g(\sigma^*)$ sub-band [1, 18]. The temperature-dependence of the ratio of these two components is presented in figure 1(d) and will be discussed in section 4.1.

3.2. EXAFS

The x-ray absorption spectra were treated following a standard data analysis procedure [15, 19]. Particular attention was devoted to the EXAFS zero-line removal through a multi-step polynomial/cubic-spline procedure [19], in order to have a correct behaviour of the EXAFS signal from the first shell. The extracted extended x-ray absorption fine structure (EXAFS) spectra $\chi(k)k^2$ and their Fourier transforms (FT) are shown in figure 3. A significant decrease in the peaks' amplitudes with increasing thermal disorder is well visible in figure 3(b); however, on the whole, the shape both of the EXAFS signals and of their FTs remains similar with the exception of the highest temperature ($T = 668$ K) spectrum. Note that the positions of peaks in the FTs are shifted from their true crystallographic values because the FTs were calculated without phase-shift correction.

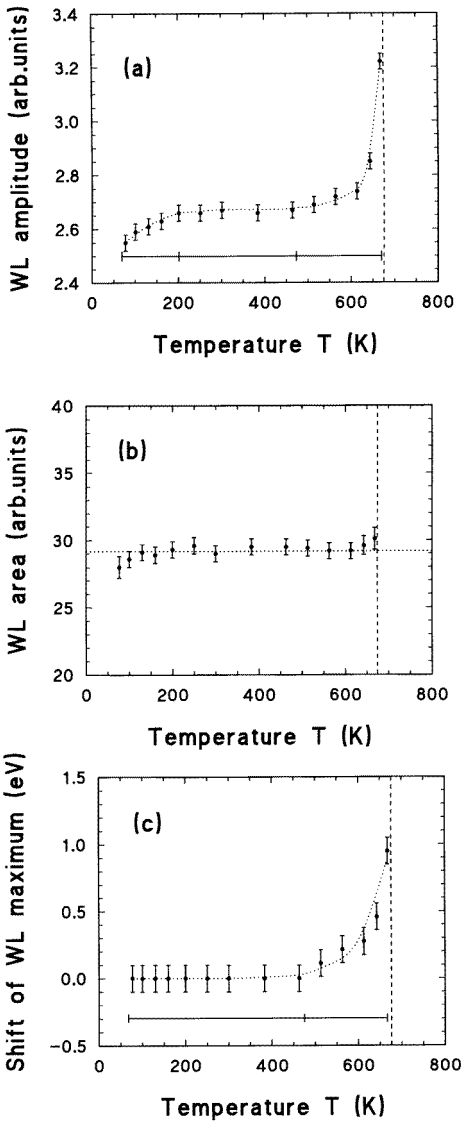

Figure 2. The temperature-dependence of the white-line (WL) amplitude (a), the area under the WL (b) and the position of the WL maximum (c). Dotted lines are guides for the eye. The vertical broken line shows the ReO_3 decomposition temperature $T_d \simeq 673$ K [16].

The attribution of peaks in the FTs to different coordination shells was described by two of us previously [13, 14]. Here we will focus our attention only on the two peaks located at 0.7–1.9 and 4.4–5.5 Å, whose low-temperature structural data were presented earlier [15]. These peaks are mainly due to the first shell (O_1) and the fourth shell (Re_4) contributions, respectively; however, the outer 30 oxygen atoms (O_5) of the fifth shell, located in the undistorted ReO_3 structure at $R(\text{Re–O}_5) \simeq 5.63$ Å from the absorber, also produce some contribution to the second peak [13–15]. Among the remaining two peaks at 2.1–3.2 and 3.2–4.0 Å only the latter has a simple structural origin: it corresponds to the contribution

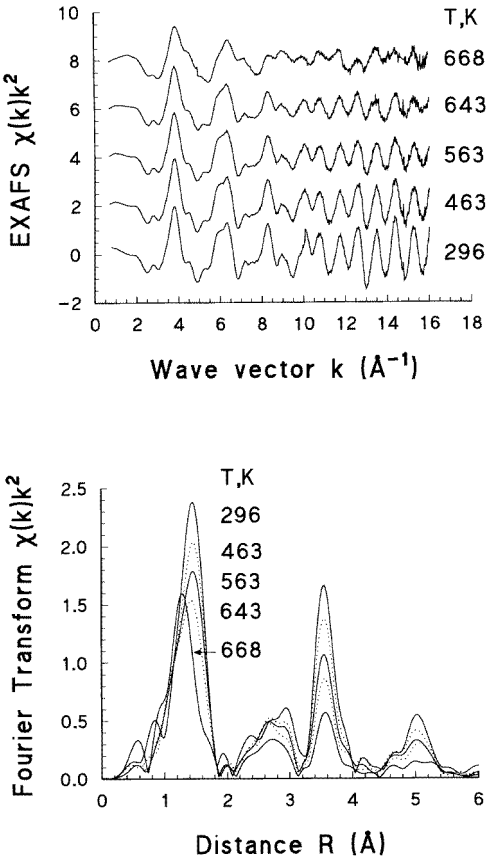

Figure 3. The temperature-dependence of the experimental EXAFS $\chi(k)k^2$ spectra measured at the Re L_3 edge in ReO_3 (upper panel) and their Fourier transforms (FTs) (lower panel). Only five spectra are shown for clarity. Note that no large changes occur in $\chi(k)k^2$ and in their FTs below about 668 K except for the continuous increase in thermal disorder, leading to the damping of the EXAFS signals' amplitude and to the decrease in the FT peaks' magnitudes. However, a shift of the position of the first shell occurs at $T = 668$ K (see lower panel).

from the rhenium atoms (Re_2) of the second shell and from the oxygen atoms (O_3) of the third shell [13, 14]. However, the EXAFS signal from the intense peak at about 3.5 Å is strongly influenced by the multiple-scattering (MS) due to six Re–O_1–Re_2 atom chains that complicates its quantitative analysis [13, 14]. Note only that qualitative analysis of this signal shows that its total phase remains nearly unchanged up to $T = 643$ K but its amplitude decreases significantly when the temperature increases. Thus, only the EXAFS signals of the first (at about 1.4 Å) and fourth (at about 5.0 Å) peaks, singled out by the back-FT procedure, were utilized in further analysis.

The first-shell EXAFS signals were analysed using several models of different complexity and flexibility. The first model (model 1) corresponds to the standard one-shell harmonic approximation in which the radial distribution function (RDF) of the absorber–backscatterer distance has a Gaussian shape [20]:

$$\chi_{model\,1}(k) = [N/(kR^2)]f_{ref}(\pi, k)\,\exp(-2\sigma^2k^2)\sin[2kR + \phi_{ref}(\pi, k)]. \quad (2)$$

Here $k = [(2m_e/\hbar^2)\Delta E]^{1/2}$ is the photoelectron wavevector ($\Delta E = E - E_0$ is the photoelectron kinetic energy), N the coordination number, R the interatomic distance and σ^2 the mean square relative displacement (MSRD) (or the EXAFS Debye–Waller (DW) factor) related to the thermal and static disorder. $f_{ref}(\pi, k)$ and $\phi_{ref}(\pi, k)$ are the total scattering amplitude and phase-shift functions of the photoelectron which were extracted from the reference EXAFS spectrum measured at low-temperature ($T = 77$ K) [15]. Note that $f_{ref}(\pi, k)$ includes the mean free path (MFP) $\lambda(k)$ correction and the multi-electron amplitude reduction factor S_0^2. The use of the experimental amplitude $f_{ref}(\pi, k)$ and phase-shift $\phi_{ref}(\pi, k)$ functions in (2) and (3) leads to relative values of the determined structural parameters. However, since ReO_3 at $T = 77$ K (used as a reference) can be considered harmonic to a good approximation [15], we set $N(77\ \text{K}) = 6$, $R_{Re-O}(77\ \text{K}) = 1.8737$ Å [21] and $\sigma^2_{Re-O}(77\ \text{K}) = 1.83 \times 10^{-3}$ Å^2 [15]. Therefore all the data extracted at higher temperatures ($T > 77$ K) have the *absolute* values.

The second model (model 2) represents a model-independent approach to the reconstruction of the RDF $G(R)$ from EXAFS. It will be described here only briefly (the details can be found in [19, 22]). For an arbitrary RDF $G(R)$ the first-shell EXAFS is given by [23]

$$\chi_{model\,2}(k) = f_{ref}(\pi, k) \int_{R_{min}}^{R_{max}} \frac{G(R)}{kR^2} \sin[2kR + \phi_{ref}(\pi, k)]\,\mathrm{d}R \tag{3}$$

where the RDF $G(R)$ corresponds to the number of atoms located in the spherical shell around the photo-absorber between R and $R + \mathrm{d}R$. Our problem is to reconstruct $G(R)$ starting from an experimental signal $\chi_{exp}(k)$ which is limited in the interval $(k_{min}; k_{max})$ and affected by systematic and statistical uncertainties.

A functional relationship exists between $\chi(k)$ and $G(R)$ within the Fourier theory formalism [24]: if $\chi(k)$ is given in k-space from 0 to k_{max} with a step $\mathrm{d}k$, then $G(r)$ is defined in r-space from 0 to $r_{max} \simeq \pi/(2\ \mathrm{d}k)$ with a spatial resolution $\delta r = 1/(2k_{max})$ (for example $\delta r \simeq 0.03$ Å for $k_{max} = 16$ Å^{-1}) [25]. Therefore, let us define an *arbitrary* RDF $G(R)$ on a grid from R_{min} to R_{max} with a step $\mathrm{d}R \simeq \delta r$. To find the shape of $G(R)$, we consider the standard least-squares problem for the EXAFS function $\chi_{model2}(k)$, defined by (3),

$$\|\chi_{model\,2}(k)k^n - \chi_{\mathrm{exp}}(k)k^n\|^2 \tag{4}$$

where k^n is the weighting factor with n being a positive number (n was set to 2 in the present work). Note also that the shape of the starting RDF influences only the time of convergence to the solution and does not affect the final result since, if the algorithm described below is run for sufficiently long, it will eventually lead to the same RDF $G(R)$ being in best agreement with experimental data.

Since the experimental EXAFS signal $\chi_{exp}(k)$ is limited in k-space, it is convenient to discuss the influence of the k_{min} and k_{max} values on the determination of the RDF $G(R)$. The low-k limit, $k_{min} > 0$, leads to limitations on the information about strongly broadened and long-distance parts of the RDF whose contribution to the EXAFS signal is restricted to the range $(0; k_{min})$. If inversion of (3) is perfomed directly, the limit k_{min} introduces spurious variations in $G(R)$ due to the abrupt change in χ_{exp} at k_{min} under the integration [25]. Note that the value of $n = 2$ in (4) was chosen in such a way as to make the weight of the low-k part ($k < k_{min} = 2$ Å^{-1}) of the EXAFS spectrum small enough compared to the other part used in the fit. However, the absence of the low-k information limits the accuracy of the obtained RDF in any case. The high-k limit, $k_{max} = 14$ Å^{-1}, is responsible for the resolution of the obtained RDF (see above). Besides, if inversion of (3) is performed

directly, as in the splice method [25], the abrupt change in χ_{exp} at k_{max} leads to truncation problems in the Fourier transform, resulting in the appearance of spurious variations in $G(R)$ [19]. In the present approach, the last difficulty has been overcome, because the integration was performed over $G(R)$ instead of χ_{exp}: the large separation between the first and the second shell in ReO_3 implies that the RDF for the first shell $G(R)$ tends to zero when $R \to R_{min}$ and $R \to R_{max}$.

Two numerical approaches [22, 19] exist to solve the problem (4) and, thus, to find the RDF $G(R)$ which best reproduces the experimental signal $\chi_{exp}(k)$. The first approach, used in the present work, is based on the iterative solution of (4) with an additional requirement on the smoothness of $G(R)$ [19]. The criterion of smoothness is realised via a standard nonlinear seven-point smoothing algorithm based on a third-order polynomial function. The smoothing is performed at each step of the iteration procedure, continuously keeping the smooth shape of the RDF during the fit. Such a procedure plays the role of a high-frequency filter, allowing one to exclude situations in which sharp artificial peaks and side lobes [22] may grow in $G(R)$ due to the noise present in $\chi_{exp}(k)$. However, it was found that the smoothing procedure has little importance when the fit of an EXAFS signal singled out by a Fourier transform is performed. Note that this approach is similar to the regularization technique [26], with the difference that additional terms with the regularization parameters, which should appear in (4) and make the problem solvable using the methods of linear algebra within the regularization approach [26], are substituted by the smoothness constraint on the shape of $G(R)$ and then the problem (4) is solved using an iterative procedure [19]. This approach was tested on a set of model distributions [19] and was successfully applied to the analysis of a number of crystalline compounds such as WO_{3-x}, MoO_3, $W(Mo)O_3 \cdot nH_2O$ and $Mo_xW_{1-x}O_3$ [19, 27].

The second approach corresponds to a method [22] similar to the one-dimensional reverse Monte Carlo (RMC) technique [28] in which the final RDF is found by the successive raising and lowering of $G(R)$ within each dR interval until the best agreement between $\chi_{model}(k)$ and $\chi_{exp}(k)$ has been achieved. This approach was applied recently to disordered systems [22].

The RDF $G(R)$ obtained by method 2 can be directly compared with that obtained by other experimental techniques or computer simulations. However, it is often useful for comparison with the results of other techniques to have a set of structural parameters instead of a total distribution function. Therefore a parametrization of the obtained RDF using a proper analytical model can be performed. In the simplest case, a decomposition into a set of Gaussians can be performed, leading to results close to those which can be obtained by a standard multi-shell least-squares fitting approach. The advantages of method 2 in comparison to the multi-shell fit are as follows: first, the number of shells and their positions can be chosen in a more adequate way, depending on the shape of the obtained RDF; second, the obtained structural information is less sensitive to the low-frequency non-structural oscillations (due to the inaccuracies of the EXAFS background removal and the possible presence of atomic-like oscillations [29]) which are often present in the experimental $\chi(k)$ data even after the Fourier filtering procedure [19]. It is necessary to point out that, if parametrization is performed, one should take into account the total number of parameters used in the model: it must be less than that given by the Nyquist theorem [30, 31]

$$M_{max} \simeq (2\Delta k \Delta R)/\pi + 2 \tag{5}$$

where Δk and ΔR are respectively the widths in k- and in r-space used in the Fourier filtering procedure. For the first shell of rhenium in ReO_3, $\Delta k = 12$ Å^{-1} and $\Delta R = 1.3$ Å

so that $M_{max} \simeq 12$. Note that an approximate relationship exists between M_{max} and the number of points $M_r = \Delta R/\mathrm{d}R + 1$ in which $G(R)$ is defined in r-space:

$$M_{max} \simeq (M_r - 1)/\pi + 2 \tag{6}$$

where the following approximations are used: $\Delta k \simeq k_{max}$ and $\mathrm{d}R \simeq 1/(2k_{max})$.

Besides the two above-mentioned methods, the standard multi-shell fitting procedure within the single-scattering harmonic approximation (method 3) [20, 23] and the splice technique (method 4) [25, 32] were also applied in the present work to the analysis of the first-shell EXAFS signal. The results obtained by method 3 agree quite well with the results of method 2. However, due to the above-discussed disadvantages of method 3, the obtained structural parameters have larger error bars. The application of the model-independent splice technique (method 4) [25, 32] gives RDFs which are more noisy than those obtained by using method 2. This can be explained in terms of the reason mentioned above [19]: the thermal MSRD value for the Re–O pair in the first shell is small enough (even at high temperatures) to result in the high amplitude of the EXAFS signal at k_{max}; consequently, the so-called *truncation* effect [24] occurs in the calculation of the integral over the reduced EXAFS signal within the splice approach [25] that leads to the appearance in the RDF of a set of spurious peaks.

The EXAFS signals from the fourth peak at about 5.0 Å were analysed in the same way as previously [15]. We used a two-shell single-scattering harmonic approximation in which the RDF related to the fourth peak consists of the sum of two Gaussians corresponding to the groups of 12 rhenium (Re_4) and 30 oxygen (O_5) atoms. The EXAFS signal of each of the two shells was calculated by equation (2) with backscattering amplitude and phase functions obtained theoretically using the FEFF code [15, 33]. The values of coordination numbers and interatomic distances were fixed at their crystallographic values ($N(Re_4)$=12, $R(Re–Re_4) =$ 5.30 Å, $N(O_5) = 30$ and $R(Re–O_5) = 5.63$ Å). Only the MSRDs σ^2 of Re–O_5 and Re–Re_4 pairs were used as fitting parameters, satisfying completely the Nyquist criterion for the fourth shell of rhenium in ReO_3: $M_{max} \simeq 10$ at $\Delta k = 12$ Å^{-1} and $\Delta R = 1.1$ Å.

4. Results

4.1. XANES

The results of the XANES analysis, described in section 3.1, are presented in figures 1(c) and (d) and 2. The formal valence state of the rhenium ion in ReO_3 is 6+, therefore it has a [Xe]$5d^1$ ground state configuration. At the Re L_3 edge, following the dipole transition rule $\Delta l = \pm 1$, a $2p_{3/2}$(Re) core electron is excited to an empty quasi-bound $\overline{5, \epsilon}$d state in the continuum (ϵ) with 5d(Re) atomic character and the final state is described as $2p^5 5d^2$ [34]. This transition gives the origin of the WL (figures 1(a) and (b)). The second possible channel $2p_{3/2}(\mathrm{Re}) \rightarrow \overline{6, \epsilon}$s was found to be smaller by a factor of about 50 [13], therefore we have neglected it in the further analysis. The bar over $\overline{5, \epsilon}$d and $\overline{6, \epsilon}$s indicates that the final state of the photoelectron is the relaxed excited state in the presence of the core hole at the 2p level screened by other electrons.

The integral intensity of the WL (the WL area) is proportional to the squared radial matrix element times the number of empty 5d states: it remains constant in the whole range of temperatures except for very low ($T < 130$ K) and high ($T > 600$ K) temperatures (figure 2 (middle panel)). However, the WL amplitude increases with temperature (figures 1(b) and 2 (upper panel)) and a shift of the WL maximum to higher energies occurs at $T > 470$ K (figures 1(a) and 2 (lower panel)).

The following discussion will be based on a single-particle model taking into account the 2p core spin–orbit coupling and the crystal field splitting $\Delta_{5d} \simeq 6.5$ eV [18] (4.7 eV [35]) of the 5d conduction band. Other effects such as 5d spin–orbit coupling ($\Delta_{so} \simeq 1.5$ eV [1]), correlations within the 5d band and the correlations between the 2p core hole and the 5d holes are considered to be smaller [36] and will not be discussed here.

In the initial state, the 5d conduction band is split by the ligand field of six oxygen atoms into the sub-band $t_{2g}(\pi^*)$, a sixth of which is filled, and the completely empty sub-band $e_g(\sigma^*)$ [1, 18, 35]. There are five and four unoccupied states in the $t_{2g}(\pi^*)$ and $e_g(\sigma^*)$ sub-bands, respectively. The $t_{2g}(\pi^*)$ sub-band is characterized by a sharper density of states compared to $e_g(\sigma^*)$ [18]: this situation is in agreement with the two-Gaussian (G_t and G_e) decomposition shown in figure 1(c). In the final state, which is actually observed, the separation between the $t_{2g}(\pi^*)$ and $e_g(\sigma^*)$ sub-bands is modified due to their different relaxations in the presence of the core hole [37]. Note that the separate transitions into the non-bonding $t_{2g}(\pi^*)$ and antibonding $e_g(\sigma^*)$ states are not observed directly in the experiment (figure 1(a)) due to the large core-hole level width Γ_{L_3}(Re)=3.4 eV [38] and the experimental broadening. They can be found only by decomposition of the WL into two Gaussian components (G_t and G_e) (see figure 1(c)) (as has been mentioned in section 3.1, no one single Gaussian or Lorentzian distribution is sufficient to describe the WL shape).

The increase in temperature leads to modifications both of G_t and of G_e components: (i) the positions of their maxima shift to higher energies by about 0.7–0.8 eV; (ii) the FWHMs decrease by about 1.2 and about 3.9 eV for the G_t and G_e curves, respectively, and (iii) the amplitude of the G_t component decreases slightly while it increases strongly for the G_e component. Besides, the ratio G_t/G_e

$$G_t/G_e \simeq |\langle t_{2g}(\pi^*)|\hat{\epsilon}\cdot\boldsymbol{r}|2p_{3/2}\rangle|^2 N_{t_{2g}(\pi^*)}(E)/|\langle e_g(\sigma^*)|\hat{\epsilon}\cdot\boldsymbol{r}|2p_{3/2}\rangle|^2 N_{e_g(\sigma^*)}(E) \tag{7}$$

decreases continuously with increasing temperature, indicating a strong and progressive localization of the electron states within the two sub-bands occurring with temperature (figure 1(d)): at high temperature ($T \simeq 600$ K), the ratio G_t/G_e is close to that in the pure atomic case ($N_{t_{2g}(\pi^*)}(E)/N_{e_g(\sigma^*)}(E) = \frac{5}{4}$) (see the broken line in figure 1(d)).

These results indicate that the increase of temperature leads to the narrowing of the $t_{2g}(\pi^*)$ and $e_g(\sigma^*)$ sub-bands with a strong localization of the electron states (especially of those having e_g character) at rhenium sites due to the electron–phonon coupling [1]. Moreover, a shift in the position of the WL (or G_t and G_e) maximum allows us to suppose that the effective charge of the rhenium ions increases with temperature due to the decrease of the rhenium–oxygen pd covalent mixing. As a result of the localization, it is expected that, at high temperature, a distortion of the local rhenium environment should occur due to the Jahn–Teller effect. For the d^1 configuration [39] of Re^{6+} ions, the regular ReO_6 octahedra should become compressed with two short and four long Re–O distances.

4.2. EXAFS: the first shell

The first-shell contributions to the experimental EXAFS signals were analysed following the procedures described in section 3.2. The best-fit results obtained using models 1 and 2 are presented in figure 4.

The low-temperature data ($T < 350$ K) have been interpreted well previously using the standard one-shell Gaussian model (model 1) [15]. At higher temperatures, however, the quality of the fit decreases with increasing temperature: the simple model 1 is able to reproduce the experimental data only up to $k \simeq 9$ Å^{-1}, giving worse results at large wavevector values (figure 4(a)). This means that, at high temperatures thermal disorder or

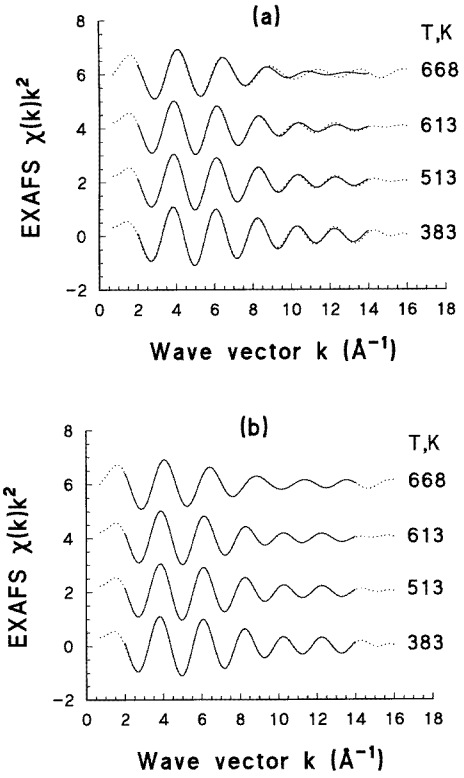

Figure 4. Best fits (full lines) of the experimental EXAFS $\chi(k)k^2$ signals of the first shell (dotted lines) at different temperatures using two models described in the text: (a) a one-shell harmonic model (model 1) and (b) a model-independent RDF approach (model 2). Only four spectra are shown for clarity.

static distortions influence the distribution of Re–O distances which strongly deviates from the Gaussian one. Model 1 is anyway suitable to extract an average behaviour of structural parameters (figure 5) and, besides, it is very stable numerically due to the small number (three) of fitting parameters (N, R and σ^2).

The results obtained by using model 1 show that the number of oxygen atoms in the first shell of rhenium is always equal to six (upper panel in figure 5). However, a decrease in the average Re–O distance from the value given by XRD [21] occurs at $T > 600$ K (middle panel in figure 5). Besides, a strong deviation of the MSRD σ^2 from the Debye model ($\Theta_D = 780$ K [15]) occurs already at $T > 350$ K (lower panel in figure 5): we attribute this difference to the presence of the static/dynamic distortion of the ReO_6 octahedron.

Model 2 gives good agreement between experimental and calculated EXAFS signals in the whole experimental k-range (figure 4(b)). This is not surprising, since model 2 is limited only by the inaccuracies in the scattering amplitude and phase-shift functions: those used here were extracted from experimental data measured at 77 K and therefore their reliability can be considered good. In model 2, the RDF $G(R)$ is not fixed to some analytical form; therefore it can have an arbitrary shape and takes into account any kind of possible distortion, thermal as well as static [19, 22]. The obtained RDFs $G(R)$ are presented in figure 6(a). Of course, the accuracy of their shapes is limited by the lack

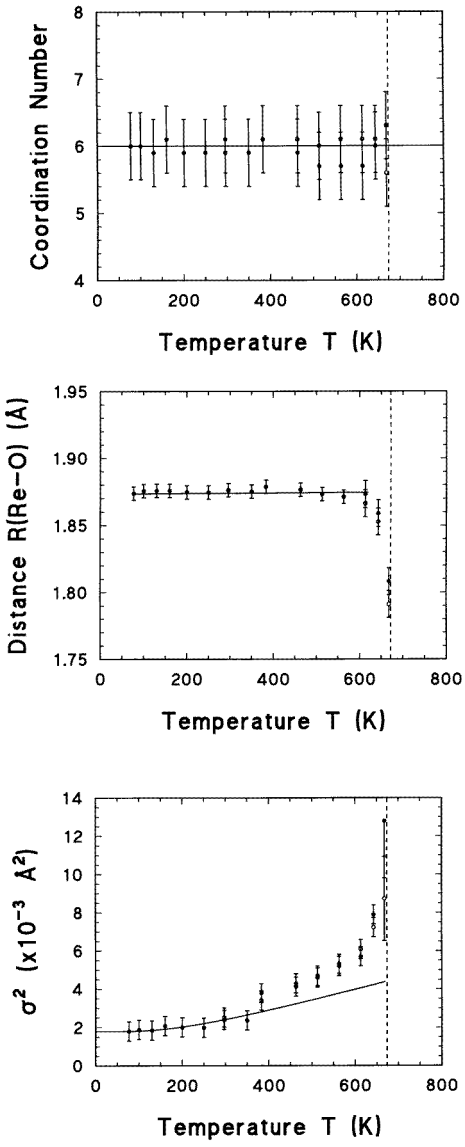

Figure 5. The temperature-dependence of the *average* coordination number $N(O_1)$ (the number of oxygen atoms), the interatomic distance $R(Re–O_1)$ and the MSRD $\sigma^2(Re–O_1)$ in the first shell of rhenium. The full and open circles show the results obtained by using models 1 and 2, respectively. Full lines correspond to $N = 6$, the interatomic distance given by diffraction [10, 21] and the MSRD given by the Debye model with $\Theta_D = 780$ K [15]. The vertical broken line shows the ReO_3 decomposition temperature $T_d \simeq 673$ K [16]. Note a decrease in the average $Re–O_1$ distance at $T > 600$ K and a large deviation of the MSRD from the Debye model occurring at $T > 350$ K.

of $k < k_{min}$ and $k > k_{max}$ information (see section 3.2). The RDFs have two interesting peculiarities. First, the asymmetry of the RDF begins on $T = 383$ K and increases with temperature up to 643 K: it appears as a tail on the low-R side of the distribution, whereas

for a purely thermal anharmonic pair potential, one generally expects to find a high-R tail. Second, a clear distortion of the first shell into two sub-shells occurs at 668 K (figure 6(a)). A rough single-Gaussian approximation of the RDFs in figure 6(a) gives results similar to those given by model 1 (see the open circles in figure 5).

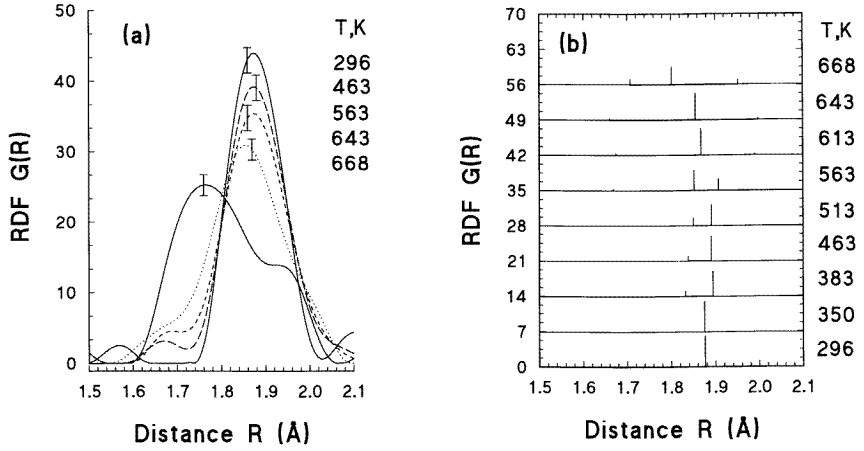

Figure 6. (a) RDF $G(R)$ for the first shell of rhenium in ReO_3 at various temperatures obtained using the model-independent RDF approach (model 2). An asymmetry in the RDF $G(R)$, consisting of the tail on the left-hand side of the peak ($R \simeq 1.7$ Å), progressively increases with temperature, the peak passing to the double-peak shape at $T = 668$ K. (b) A schematic representation of table 1. The positions R of the groups of oxygen atoms in the first shell of rhenium are shown by vertical lines. The amplitudes of the vertical lines are equal to coordination numbers N.

More refined analysis shows that, within the first approximation, the obtained RDFs for $383 \leqslant T < 563$ K can be decomposed into two Gaussians (six parameters: N_i, R_i, σ_i^2 and $i = 1, 2$) whereas for $T \geqslant 563$ K three Gaussians (nine parameters: N_i, R_i, σ_i^2 and $i = 1, 2, 3$) (table 1 and figure 6(b)). Such parametrization of the model-independent RDFs (figure 6) satisfies the criterion given by the Nyquist theorem [30, 31] ($M_{max} \simeq 12$ in our case). To examine the significance of adding a new Gaussian component, the method based on an F-test was also used [40]. The fitting error ϵ_i between the RDF $G_{model\ 2}(R)$ obtained by method 2, and the fitted RDF $G_i^{fit}(R)$, which is equal to the sum of i Gaussians, was found to be

$$\epsilon_i = \frac{M_{max}}{M_r(M_{max} - M_{fit})} \sum_{j=1}^{M_r} (G_i^{fit}(R_j) - G_{model\ 2}(R_j))^2 \tag{8}$$

where M_r is the number of points in r-space, M_{fit} is the number of fitting parameters and M_{max} is given by equation (5). Choosing the significance level equal to 5%, the criterion of adding a Gaussian component is given by [41]

$$\epsilon_i / \epsilon_{i+1} > F_{0.95} \tag{9}$$

where the value of $F_{0.95}$ can be taken from a table (see, for example, table VII in [41]). The results of the F-test are presented in table 1: they support the numbers of Gaussian components used for the decomposition of the RDFs obtained by method 2.

The use of two Gaussians for the RDFs corresponding to the EXAFS spectra at $383 \leqslant T < 563$ K allows us to describe the low-R-side asymmetry of $G(R)$, while the

Table 1. Structural data for the local environment of rhenium in ReO_3 at $T \geqslant$ RT (see also figure 6(b)). The data were obtained by the decomposition of the RDF $G(R)$ into one, two or three Gaussian-like sub-shells representing symmetry-inequivalent groups of oxygen atoms within the first coordination shell. The Schoenflies symbol for the rhenium site symmetry group is given in the second column. The fitting errors ϵ_i are calculated by equation (8) and the values of Fisher's quantity $F_{0.95}$ are taken from table VII of [41]. The errors of structural parameters are $\Delta N \simeq \pm 0.3$, $\Delta R \simeq \pm 0.005$ Å and $\Delta\sigma^2 \simeq \pm 0.0005$ Å^2.

		One sub-shell			Two sub-shells			Three sub-shells				
T(K)	Space group	N_1	R_1 (Å)	σ_1^2 (Å^2)	N_2	R_2 (Å)	σ_2^2 (Å^2)	N_3	R_3(Å)	σ_3^2 (Å^2)	$\epsilon_i/\epsilon_{i+1}$	$F_{0.95}$
RT	O_h	6.1	1.876	0.0024								
350	O_h	5.9	1.875	0.0024								
383		4.9	1.894	0.0033	1.1	1.832	0.0014				5.3	4.8
463		4.9	1.890	0.0042	1.0	1.838	0.0019				6.3	4.8
513	D_{4h}	4.2	1.891	0.0050	1.6	1.850	0.0027				55.8	9.8
563		3.7	1.862	0.0040	2.1	1.9169	0.0057	0.3	1.678	0.0012	10.3	9.8
613		5.3	1.868	0.0048	0.4	1.990	0.0024	0.4	1.674	0.0017	12.9	9.8
643		5.3	1.855	0.0056	0.4	1.998	0.0015	0.4	1.660	0.0023	12.5	9.8
668	C_{4v}	3.6	1.801	0.0049	1.1	1.952	0.0019	1.2	1.707	0.0019	51.1	9.8

three-Gaussian parametrization describes further broadening (the peak at about 1.67 Å in figure 6(a)) of the RDFs at higher temperatures. Note that, even if the RDF at $T = 668$ K has a double-peaked shape, the first peak at about 1.75 Å is so wide that two Gaussians are required for its description.

Thus, model 2 allows us to interpret in detail the distortion of the first shell in ReO_3, discovered within the one-shell model 1. According to the results of the analysis (see table 1), the group of six oxygen atoms surrounding the rhenium atom in the form of a regular octahedron (R(Re–O) = 1.875 Å) at $T \leqslant 350$ K are split into two and three subgroups (sub-shells) at higher temperatures. Our results show that a progressive distortion takes place so that rhenium sites having different local symmetry are present in ReO_3 at some intermediate temperatures (in $383 \leqslant T \leqslant 513$ K and $563 \leqslant T \leqslant 643$ K).

4.3. EXAFS: the fourth shell

The peak at 4.4–5.5 Å in the FT (lower panel in figure 3) corresponds to the fourth shell, composed of 12 rhenium atoms at about 5.30 Å and to the fifth shell formed by 30 oxygen atoms at about 5.63 Å. The rhenium atoms produce the main contribution for two reasons: (i) the rhenium backscattering amplitude is much larger at high energies than that of oxygen atoms and (ii) the thermal disorder (the MSRD values) of rhenium atoms is smaller than that of the oxygen atoms [15]. As a result, since the oxygen atoms contribute mainly at low-k values, it is possible to separate partially the contributions of rhenium and oxygen atoms in k-space and thus to decrease the correlation in the best-fit procedure between the structural parameters of two shells.

The EXAFS signals of the fourth shell, singled out by back-FT, were analysed using a two-shell Gaussian model containing contributions from oxygen and rhenium atoms in the same way as in [15] (see also section 3.2). The analysis shows that only the amplitude varies with temperature due to the increase in thermal disorder whereas the total phase of the EXAFS signal, related to the peak position in the FT, remains unchanged within the experimental accuracy (lower panel in figure 3). This means that the variation of the Re–

Re_4 ($R(77\ \mathrm{K}) = 5.30$ Å) distance is very small, as expected from the XRD measurements [21]: $\Delta R(\mathrm{Re–Re_4}) = R(670\ \mathrm{K}) – R(77\ \mathrm{K}) = 0.0035$ Å.

The obtained high-temperature MSRDs for the Re–Re_4 atom pair are shown in figure 7. They are in good agreement with previous low-temperature measurements and the correlated Debye model with $\Theta_D = 333$ K [15]. Note that the correlation in the atomic motion for the Re–Re_4 pair, corresponding to the difference between the dotted and full curves in figure 7, is smaller than that for the Re–O_1 pair in the first shell for reasons discussed in [15]. The MSRD for the Re–Re_4 atom pair increases with temperature according to the Debye model for $T \leqslant 643$ K. However, it has an abrupt rise at $T \simeq 668$ K (see the last point in figure 7), that can be explained in terms of the strong decrease in the correlation of the Re–Re atomic motion near the ReO_3 decomposition temperature $T_d \simeq 673$ K. This conclusion is supported by the fact that, at $T = 668$ K, the value of the MSRD σ^2(Re–Re_4) is close to the value given by the uncorrelated Debye model σ^2_{MSD} (dotted line in figure 7) equal to the sum of the mean square displacements (MSD) u^2_{Re} [15]. Therefore one can use the value of the MSRD σ^2(Re–Re_4) at $T = 668$ K to estimate σ^2_{MSD} and u^2_{Re}: $u^2_{Re} \equiv \sigma^2_{MSD}/2 \simeq 0.0053$ Å^2. Note that the value of u^2_{Re} at $T = 668$ K is more than double the room temperature MSD of rhenium atoms $u^2_{Re}(\mathrm{RT}) \simeq 0.0018$ Å^2 observed by XRD [42]. It could be interesting to compare $u^2_{Re}(T = 668\ \mathrm{K})$ estimated by EXAFS with that determined by XRD, however, the known XRD data are available only up to 300 K [42].

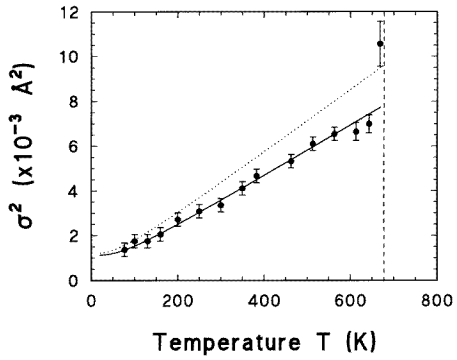

Figure 7. The temperature-dependence of the MSRD for the Re–Re_4 ($R \simeq 5.3$ Å) atom pair. Full and dotted curves correspond to the correlated and uncorrelated Debye models with $\Theta_D = 333$ K, respectively [15]. The vertical broken line shows the ReO_3 decomposition temperature $T_d \simeq 673$ K [16].

5. Discussion

In this section, on the basis of the results of x-ray absorption spectra analysis, we will discuss a model which is able to explain the behaviour of the electronic and atomic structures in ReO_3 within the temperature range 77–668 K. The perovskite-like structure of ReO_3, composed below 380 K of regular ReO_6 octahedra joined by vertices, is characterized by the strong covalent σ-bonding between rhenium and oxygen atoms involving the cationic $e_g^2 sp_\sigma^3$ and anionic sp_σ orbitals [1, 18, 35]. The presence of the strong Re–O bonds is manifested in the high anisotropy of oxygen thermal vibrations [42–44] and was recently confirmed by EXAFS measurements [15]. As a result of the strong covalent bonding, the Re–O π bonds formed by O $2p_\pi$ and Re $5d(t_{2g})$ orbitals are highly directional [1, 18]

and rhenium oxide, having a broadened conduction band with 5d character and one electron per rhenium atom, exhibits high metallic conductivity [8, 45]. The presence of an electron in the conduction band is responsible for the stability of the ReO_3 lattice since structural distortions lead to an increase in the total energy of the conduction electrons and, consequently, of the total crystal energy [7, 46]. The absence of any phase transition in ReO_3 at temperatures $T < 350$ K was confirmed by XRD [42] and EXAFS [15] studies. One should point out that, in contrast to ReO_3, tungsten oxide WO_3 has a distorted ReO_3-type structure whose symmetry changes consequently upon cooling from tetragonal $\rightarrow$ orthorhombic $\rightarrow$ monoclinic(I) $\rightarrow$ triclinic $\rightarrow$ monoclinic(II) due to the condensation in each phase of the particular soft phonon modes [46]. The formal valence of tungsten ions in WO_3 is 6+, as of rhenium ions in ReO_3. However, for tungsten this results in the $[Xe]5d^0$ ground state configuration with an empty 5d band. Thus the series of structural phase transitions observed in WO_3 is explained in terms of the inter-band screening of the phonon modes involving the empty conduction and filled valence bands [7].

The possibility of a phase transition in ReO_3 was suggested on the basis of the high anisotropy of oxygen thermal vibrations [44]: the XRD data [42] show that the amplitude of the oxygen vibrations is much larger (about 2–3 times) in the direction perpendicular to the Re–O–Re chain than it is along it. Such thermal behaviour is similar to that observed in perovskites, in which a displacive phase transitions occurs at low temperatures due to the optical mode softening [4]. However, in ReO_3, a set of phase transitions $Pm3m \rightarrow P4/mbm \rightarrow I4/mmm \rightarrow Im3$ due to the consequent condensation of one, two and three M_3 phonons, consisting of the rotation of ReO_6 octahedra around [100] axes and related to the anisotropy of the oxygen vibrations, was only found at room temperature and high pressure (above 5 kbar) [9, 10]. One should point out that a first pressure-induced transition at 5.2 kbar from the cubic $Pm3m$ to the tetragonal $P4/mbm$ phase is accompanied by a small distortion (compression) of the ReO_6 octahedra, resulting in four long $R(\text{Re–O(1)}) = 1.875$ Å and two short $R(\text{Re–O(2)}) = 1.8707$ Å distances whereas at higher pressure the ReO_6 octahedra remain undistorted with $R(\text{Re–O}) = 1.872$–1.874 Å [10]. Similar behaviour was also observed in Na_xWO_3, a metallic perovskite-type compound, in which a condensation of M_3 phonons occurs upon cooling from 500 to 3 K [12].

In the present work, based on the results of the XANES and EXAFS analyses (section 4), we obtained direct evidence that, in ReO_3, a progressive localization of the 5d states following the temperature rise is accompanied at $T > 350$ K by a distortion of the ReO_6 octahedra which increases with temperature up to the decomposition point $T_d \simeq 673$ K [16].

To explain the behaviour of the local electronic and atomic structures around rhenium atoms in ReO_3 within the temperature range 77–668 K, we propose a model (see figure 8) which is based on the electron–phonon coupling mechanism. The description of the model is presented in the following. It is known [42] that the amplitude of vibrations of the oxygen atoms in the direction perpendicular to the Re–O–Re chain (M_3 phonons [10]) increases continuously with temperature. These vibrations lead to the decrease of the overlap (and interaction) between the 5d rhenium and 2p oxygen orbitals and, besides, their effect is stronger for the σ-type bonding (lobes pointing along the Re–O bond axis) than for the π-type bonding (lobes perpendicular to the Re–O bond axis). Therefore, in the case of the antibonding $e_g(\sigma^*)$ and $t_{2g}(\pi^*)$ orbitals, which contribute to the conduction band of ReO_3, the overlap (and interaction) between the $e_g(\sigma^*)$ orbitals of the cation and the $p(\sigma^*)$ orbitals of anions should decrease with temperature faster than does the overlap (and interaction) between the $t_{2g}(\pi^*)$ orbitals of the cation and the $p(\pi^*)$ orbitals of anions. This conclusion

is consistent with the results of the XANES analysis (figures 1(c) and (d) and 2) discussed in section 4.1. The decrease in the 5d(Re)–2p(O) interaction results in the contraction of the radial extension of the atomic 5d rhenium orbitals and, consequently, in a narrowing of the t_{2g} and e_g sub-bands with the localization of the 5d electron states at rhenium sites. The decrease in the covalent mixing between rhenium and oxygen orbitals leads also to an increase in the effective charge on rhenium ions since the bonding oxygen orbitals screen less the rhenium 5d orbitals [1]. As a result, the energy of the unoccupied 5d states increases and the position of the absorption edge (or the WL maximum) shifts to higher energies (see figures 1(a)–(c) and the lower panel in figure 2). A similar effect of conduction-band narrowing due to a decrease in the cation–anion interaction was observed recently for Na_xWO_3 [47]. The analysis of the oxygen K edge showed that the presence of sodium ions (which are *randomly* distributed at the A sites of the ABO_3 lattice [1] and compete with tungsten ions for bonding to the O 2p states [1]) results in a weakening of the O 2p–W 5d interaction, leading to a reduction in the t_{2g}–e_g splitting and to the 5d band narrowing [1, 47, 48].

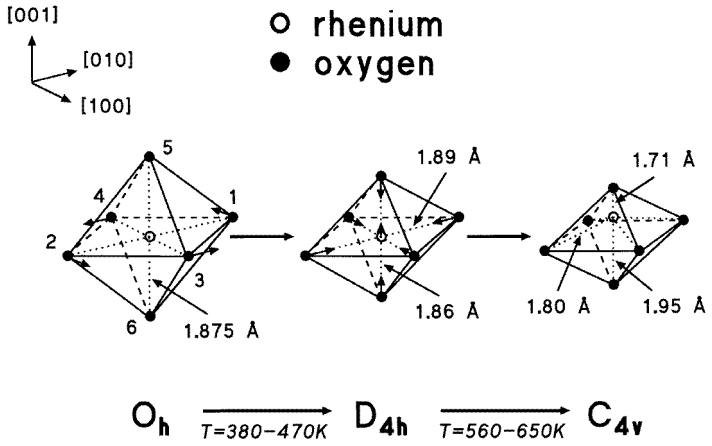

Figure 8. A model of the high-temperature behaviour of ReO_3 within the first coordination shell: the local symmetry at the rhenium site decreases consequently from O_h to D_{4h} and C_{4v}. The rhenium atom is shown by an open circle and the oxygen atoms by full circles. The displacements of oxygen atoms leading to the distortion of the first shell are shown by arrows.

Within our model, due to the progressive localization of the 5d states with increasing temperature, at $T \simeq 380$ K the 5d electrons start to behave partially as localized and the Jahn–Teller distortion of the ReO_6 octahedra occurs. For the $5d^1 \equiv t_{2g}^1$ configuration of the rhenium ion, the compressed octahedron should be energetically more favourable than is the elongated one [39]; therefore the octahedral rhenium site symmetry O_h (R(Re–O) = 1.875 Å) is lowered by the Jahn–Teller effect to the tetragonal D_{4h} with two short (1.86 Å) and four long distances (1.89 Å) (see figure 8 and table 1). Similar Jahn–Teller distortions were observed earlier in perovskite $SrTiO_3$ doped with Cr^{5+} [49] and V^{4+} [50] ions which both have the $3d^1 \equiv t_{2g}^1$ configuration with the 3d states being localized. The Jahn–Teller distortion does not displace the cations from the centres of symmetry of their anionic interstices and does not enlarge the crystallographic unit cell [1, 39]: this is in agreement with the unchanged distances between the absorber and rhenium atoms located in outer shells: the peaks corresponding to the rhenium shells in the FTs are located nearly

at the same position at $T < 668$ K and, in particular, the distance between the absorber and rhenium atoms in the fourth shell, which was analysed in the present work, remains unchanged within the accuracy of the experiment (see section 4.3). We should note that the XAS results (figures 1(c) and (d) and table 1) do not allow one to distinguish whether the localization occurs at all rhenium sites simultaneously or not. Therefore, in the range of temperatures $383 \leqslant T < 513$ K, there can be two possibilities: (i) a progressive lowering of the local symmetry at all rhenium sites occurs at the same time and (ii) both distorted (D_{4h}) and undistorted (O_h) octahedra coexist so that the obtained structural parameters give average values over the rhenium sites of both types.

Further distortion of the ReO_6 octahedron, observed from the EXAFS data at $T > 563$ K (figure 6(a)), can be explained in terms of the electron–phonon coupling of the 5d localized electrons with the $M_3'^Z$ phonons (which are responsible for a set of phase transitions in WO_3 [46]) leading to the z displacements (by about 0.12 Å) of rhenium atoms and to the lowering of the rhenium site symmetry from D_{4h} to C_{4v}. It was found (see figure 8 and table 1) that the rhenium ions located at the sites with the C_{4v} symmetry have one short (1.71 Å), four intermediate (1.80 Å) and one long (1.95 Å) Re–O distances. Also in this case, it is difficult to conclude whether the distortions at intermediate temperatures $513 < T < 668$ K occur simultaneously for all rhenium sites or not.

6. Summary and conclusions

We have presented for the first time an x-ray absorption spectroscopy study on the Re L_3 edge of the high-temperature structure of ReO_3. The measurements were performed in the temperature range from RT up to the ReO_3 decomposition temperature $T_d \simeq 673$ K [16]. Both XANES and EXAFS regions have been analysed, and their results are discussed, together with those obtained by us earlier at low temperatures ($T < 350$ K) [15].

A modification of the local electronic structure was observed with increasing temperature. It can be explained (i) in terms of a progressive narrowing of the t_{2g} and e_g sub-bands with a localization of the electron states (especially having e_g character) at rhenium sites due to the electron–phonon coupling and (ii) in terms of the increase in the effective charge on rhenium ions.

The beginning of a distortion of the ReO_6 octahedra was observed at $T \simeq 380$ K. It leads to the lowering of the local symmetry at rhenium sites from O_h to D_{4h}. This distortion is explained by the modifications occurring within the electronic structure of ReO_3 due to the Jahn–Teller effect caused by the rhenium localized $5d^1$ electron which becomes localized at high temperature. When temperature increases, at $T \simeq 563$ K, a further distortion of the ReO_6 octahedra from D_{4h} to C_{4v} local symmetry appears which can be explained in terms of the coupling of the 5d electron with the $M_3'^Z$ phonon. The obtained results suggest that the temperature-dependence of the ReO_3 conductivity at high temperatures ($500 < T < 670$ K) could deviate from its low-temperature behaviour [45].

Acknowledgments

AK and JP are grateful to H Dexpert and Ph Parent (LURE, Paris) for support during the experiments. AK and JP wish to acknowledge the partial support of this work by the Centro CNR-ITC di Fisica degli Stati Aggregati ed Impianto Ionico (Trento) and the Università di Trento. The help of M Grazioli in the comparative analysis of the EXAFS data using the cumulant-splice method is acknowledged. This work was supported in part by NATO Guest Fellowship 218.1596 and the International Science Foundation, grants LF8000 and LJ8100.

References

[1] Goodenough J B 1966 *J. Appl. Phys.* **37** 1415; 1971 *Prog. Solid State Chem.* **5** 145
[2] Harrison W A 1970 *Solid State Physics* (New York: McGraw-Hill) p 159
[3] Bednorz J G and Müller K A 1988 *Rev. Mod. Phys.* **60** 585
[4] Müller K A and Fayet J C 1991 *Structural Phase Transitions II* vol 45, ed K A Müller and H Thomas (Berlin: Springer) p 1
[5] Grüner G 1988 *Rev. Mod. Phys.* **60** 1129
[6] Biltz W, Lehrer G A and Meisel K 1932 *Z. Anorg. Allgem. Chem.* **207** 113
Meisel K 1932 *Z. Anorg. Allgem. Chem.* **207** 121
Biltz W 1933 *Z. Anorg. Allgem. Chem.* **214** 225
[7] Fujimori A and Tsuda N 1980 *Solid State Commun.* **34** 433
[8] Allen P B and Schulz W W 1993 *Phys. Rev.* B **47** 14434
[9] Axe J D, Fujii Y, Batlogg B, Greenblatt M and Di Gregorio S 1985 *Phys. Rev.* B **31** 663
[10] Jørgensen J E, Jorgensen J D, Batlogg B, Remeika J P and Axe J D 1986 *Phys. Rev.* B **33** 4793
[11] Clarke R 1977 *Phys. Rev. Lett.* **39** 1550
[12] Flynn E J 1980 *Phys. Rev.* B **21** 1105
Flynn E J, Solin S A and Shanks H R 1978 *Solid State Commun.* **25** 743
[13] Kuzmin A, Purans J, Benfatto M and Natoli C R 1993 *Phys. Rev.* B **47** 2480
[14] Kuzmin A and Purans J 1993 *J. Phys.: Condens. Matter* **5** 267
[15] Dalba G, Fornasini P, Kuzmin A, Purans J and Rocca F 1995 *J. Phys.: Condens. Matter* **7** 1199
[16] Weast R C, Astle M J and Beyer W H (eds) 1988 *Handbook of Chemistry and Physics* 69th edn (Boca Raton: CRC Press) p B-123
[17] Dalba G, Diop D, Fornasini P, Kuzmin A and Rocca F 1993 *J. Phys.: Condens. Matter* **5** 1643
[18] Mattheiss L F 1969 *Phys. Rev.* **181** 987
[19] Kuzmin A 1995 *Physica* B **208&209** 175; 1996 *EDA: EXAFS Data Analysis Software Package. User Manual* (available from the author); 1997 *J. Physique IV (France)* at press
[20] Lee P A, Citrin P H, Eisenberger P and Kincaid B M 1981 *Rev. Mod. Phys.* **53** 769
[21] Chang T S and Trucano P 1978 *J. Appl. Cryst.* **11** 286
[22] Kizler P 1991 *Proc. 6th Int. Conf. on x-ray Absorption Fine Structure (York)* ed S S Hasnain (Singapore: Ellis Horwood) p 78
[23] Stern E A and Heald S M 1983 *Handbook of Synchrotron Radiation* ed Koch E E (New York: North-Holland) ch 10
[24] Lanczos C 1956 *Applied Analysis* (Englewood Cliffs, NJ: Prentice-Hall)
[25] Stern E A, Ma Y, Hanske-Petitpierre O and Bouldin C E 1992 *Phys. Rev.* B **46** 687
[26] Babanov Yu A, Vasin V V, Ageev A L and Ershov N V 1981 *Phys. Status Solidi* b **105** 747
Ershov N V, Ageev A L, Vasin V V and Babanov Yu A 1981 *Phys. Status Solidi* b **108** 103
Bakushinsky A and Goncharsky A 1994 *Ill-Posed Problems: Theory and Applications* (Dordrecht: Kluwer)
[27] Purans J, Kuzmin A, Parent Ph and Dexpert H 1995 *Physica* B **208&209** 307, 373, 707
[28] McGreevy R L 1993 *Proc. ILL/ESRF Workshop on Methods in the Determination of Partial Structure Factors of Disordered Matter by Neutron and Anomalous X-Ray Diffraction* ed J B Suck *et al* (Singapore: World Scientific) p 208
[29] Rehr J J, Booth C H, Bridges F and Zabinsky S I 1994 *Phys. Rev.* B **49** 12 347
[30] Brigham E O 1974 *The Fast Fourier Transform* (Englewood Cliffs, NJ: Prentice-Hall)
[31] Stern E A 1993 *Phys. Rev.* B **48** 9825
[32] Dalba G, Fornasini P and Rocca F 1993 *Phys. Rev.* B **47** 8502
[33] Rehr J J, Mustre de Leon J, Zabinsky S I and Albers R C 1991 *J. Am. Chem. Soc.* **113** 5135
Mustre de Leon J, Rehr J J, Zabinsky S I and Albers R C 1991 *Phys. Rev.* B **44** 4146
[34] Balerna A, Bernieri E, Burattini E, Kuzmin A, Lusis A, Purans J and Cikmach P 1991 *Nucl. Instrum. Methods* A **308** 240
Kuzmin A and Purans J 1993 *J. Phys.: Condens. Matter* **5** 2333
[35] Tsukada M, Tsuda N and Minami F 1980 *J. Phys. Soc. Japan* **49** 1115
Tsukada M 1980 *J. Phys. Soc. Japan* **49** 1183
[36] Thole B T and van der Laan G 1988 *Phys. Rev.* B **48** 3158
Lever A B P 1984 *Inorganic Electronic Spectroscopy* (Amsterdam: Elsevier)
[37] Borg A, King P L, Pianetta P, Lindau I, Mitzi D B, Kapitulnik A, Soldatov A V, Della Longa S and Bianconi A 1992 *Phys. Rev.* B **46** 8487
[38] Sevier K D 1972 *Low Energy Electron Spectrometry* (New York: Wiley)

[39] Schläfer H L and Gliemann G 1969 *Basic Principles of Ligand Field Theory* (New York: Wiley)
[40] Fisher R 1956 *Statistical Methods and Scientific Inference* (Edinburgh: Oliver and Boyd)
[41] Pustyl'nik E I 1968 *Statistical Methods of Analysis and Evaluation of Measurements* (Moscow: Izd Nauka) p 230 (in Russian)
[42] Morinaga M, Sato K, Harada J, Adachi H, Ohba S and Saito Y 1983 *J. Phys. C: Solid State Phys.* **16** L177
[43] Benner R E, Brody E M and Shanks H R 1977 *J. Solid State Chem.* **22** 361
Tsuda N, Sumino Y, Ohno I and Akahane T 1976 *J. Phys. Soc. Japan* **41** 1153
[44] Pearsall T P and Coldren L A 1976 *Solid State Commun.* **18** 1093
[45] Pearsall T P and Lee C A 1974 *Phys. Rev.* B **10** 2190
King C N, Kirsch H C and Geballe T H 1971 *Solid State Commun.* **9** 907
Tanaka T, Akahane T, Bannai E, Kawai S, Tsuda N and Ishizawa Y 1976 *J. Phys. C: Solid State Phys.* **9** 1235
[46] Hirose T 1980 *J. Phys. Soc. Japan* **49** 562
[47] Kielwein M, Saiki K, Roth G, Fink J, Paasch G and Egdell R G 1995 *Phys. Rev.* B **51** 10 320
[48] Egdell R G and Hill M D 1982 *Chem. Phys. Lett.* **85** 140
Hill M D and Egdell R G 1983 *J. Phys. C: Solid State Phys.* **16** 6205
[49] Müller K A and Blazey K W 1993 *Solid State Commun.* **85** 381
de Jong H J and Glasbeek M 1976 *Solid State Commun.* **19** 1197; 1978 *Solid State Commun.* **28** 683
[50] Kool Th W and Glasbeek M 1979 *Solid State Commun.* **32** 1099; 1991 *J. Phys.: Condens. Matter* **3** 9747